Regimes of Convective Self-Aggregation in Convection-Permitting Beta-Plane Simulations

Jacob D. Carstens,[a,b] Allison A. Wing,[a]

[a] *Department of Earth, Ocean, and Atmospheric Science, Florida State University, Tallahassee, Florida, USA*

[b] *Department of Meteorology and Atmospheric Science, The Pennsylvania State University, University Park, Pennsylvania, USA*

Corresponding author: Jacob Carstens, jdcarstens17@gmail.com

Jacob Carstens' current affiliation: Penn State University

ABSTRACT: The spontaneous self-aggregation (SA) of convection in idealized model experiments highlights the importance of interactions between tropical convection and the surrounding environment. The authors have shown that SA fundamentally changes with the background rotation in previous f-plane simulations, both in terms of the resulting forms of organized convection, and the relative roles of the physical feedbacks driving them. This study considers the dependence of SA on rotation in one large domain on the β-plane, introducing an additional layer of complexity. Simulations are performed with uniform thermal forcing and explicit convection. Focuses include statistical and structural analysis of the convective modes, process-oriented diagnostics of how they develop, and resulting mean states. Two regimes of SA emerge within the first 15 days, separated by a critical zone where f is analogous to 10-15° latitude. Organized convection at near-equatorial values of f primarily consists of convectively-coupled Kelvin waves. Wind speed-surface enthalpy flux feedbacks are the dominant process driving moisture variability early on, then clear-sky shortwave radiative feedbacks are strongest in wave maintenance. In contrast, at higher f, numerous tropical cyclones develop and co-exist, dominated by surface flux and longwave processes. Tropical cyclogenesis is most pronounced at intermediate f (analogous to 25-40°), but are longer-lived at higher f. The resulting modes of SA at low f differ between these β-plane simulations (convectively-coupled waves) and prior f-plane simulations (weak tropical cyclones or non-rotating clusters). Otherwise, these results provide further evidence for the changing roles of radiative, surface flux, and advective processes in influencing SA as f changes, as found in our previous study.

SIGNIFICANCE STATEMENT: In model simulations, convection often self-organizes due to interactions with its surrounding environment. These interactions are relevant in the real-world organization of rainfall and clouds, and may thus be useful to understand for improved prediction of tropical weather and climate. Previous work using a set of simple model experiments with constant Coriolis force showed that at different latitudes, different processes dominate, and different types of organized convection result. This study verifies that finding using a more complex and realistic model, where the Coriolis force varies within the domain to resemble different latitudes. Specifically, the convection here self-organizes into atmospheric waves (periodic disturbances) at low latitudes, and tropical cyclones at high latitudes.

1. Introduction

Systems of organized convection are fundamental to tropical weather and climate. These encompass many spatial scales, including mesoscale convective systems (Houze 2004), synoptic-scale features such as tropical waves (Kiladis et al. 2009) and tropical cyclones (Emanuel 2003), and planetary-scale oscillations (Madden and Julian 1971). Organized convection also couples to the moisture, circulation, and radiation of the surrounding environment, consequently influencing tropical and global climate (Khairoutdinov and Emanuel 2010; Wing 2019). Numerous studies using simple, idealized models have shed light on many of the convection-environment interactions contributing to convective organization. Specifically, the spontaneous self-aggregation (SA) of convection from radiative-convective equilibrium (RCE) (Manabe and Strickler 1964) has revealed mechanisms relevant to real-world convective organization (Held et al. 1993; Tompkins and Craig 1998; Bretherton et al. 2005; Muller and Held 2012; Craig and Mack 2013; Wing and Emanuel 2014; Coppin and Bony 2015; Hohenegger and Stevens 2016; Holloway and Woolnough 2016; Wing and Cronin 2016; Yang 2018a,b; Patrizio and Randall 2019; Windmiller and Craig 2019; Yanase et al. 2020). These mechanisms include differential radiative cooling between cloudy and clear areas, differential surface enthalpy fluxes, and radiatively-driven mesoscale circulations.

While much of the SA literature has focused on the non-rotating space, rotating RCE environments often yield tropical cyclones (TCs) and provide insight into TC genesis, structure, size, and intensity (Bretherton et al. 2005; Nolan et al. 2007; Held and Zhao 2008; Khairoutdinov and Emanuel 2013; Zhou et al. 2014; Davis 2015; Reed and Chavas 2015; Boos et al. 2016; Merlis et al. 2016; Wing et al. 2016; Zhou et al. 2017; Muller and Romps 2018; Cronin and Chavas 2019; Wang et al. 2019; Ramsay et al. 2020; Ramirez Reyes and Yang 2021). Spontaneous TC formation in this setting is particularly interesting for genesis studies, as it captures upscale convective growth into a TC without a clear precursor disturbance. Carstens and Wing (2020) (hereafter CW20) introduced a spectrum of rotating f-plane simulations to examine TC genesis processes, spanning effective latitudes of 0.1-20°. The resulting modes of organized convection, as well as the physical pathways to TC genesis, varied markedly as a function of the background Coriolis parameter (f). Carstens and Wing (2022) (hereafter CW22) confirmed using process-oriented diagnostics that the relative roles of the mechanisms contributing to SA varied systematically with f. A critical threshold of f separated two well-defined regimes of SA in that model configuration. The "low-f" regime resembled non-rotating SA, triggered by differential surface enthalpy fluxes and maintained by radiative feedbacks. A single non-rotating cluster resulted, either in circular or banded geometry. Unlike non-rotating SA, circular patches of convection then underwent TC genesis via a "bottom-up" vortex generation pathway marked by vorticity development originating in the lowest levels, then continuing through the middle troposphere (CW20). Beyond about 5° effective latitude, SA was halted by increased dynamic export of moist static energy from regions of deep convection (a negative advective feedback). However, as f continued to increase beyond about 8°, a "top-down" TC genesis process eventually took place where vortex development originated in the middle troposphere, and the surface flux and radiative feedbacks caused by the TC helped to dry the surrounding environment. This resulted in an aggregated state that was comparable to the low-f regime, in terms of the spatial variance of moist static energy.

While powerful to isolate the role of rotation on convective processes, Cartesian f-plane simulations lack the real-world meridional variation of f (β), which has implications for various forms of tropical convection. TCs are a key example, where advection of planetary vorticity by the TC circulation causes a poleward and westward steering influence (Holland 1983), and β is shown to affect TC structure and intensity (Fang and Zhang 2012), size (Lu and Chavas 2022), and minimum distance from the equator (Chavas and Reed 2019). β is also essential to the development and propagation of equatorial waves (Matsuno 1966; Gill 1982; Kiladis et al. 2009). Thus, incorporating β into the framework of CW20 and CW22 is a natural next step in the model hierarchy, adding one additional layer of complexity to study the dependence of SA on rotation. This type of simulation requires a much larger domain, but should accommodate non-rotating and rotating modes of convection simultaneously. Indeed, aquaplanet simulations under uniform thermal forcing have shown latitudinally-dependent regimes of organized convection, including tropical cyclones and equatorial waves that develop spontaneously (Shi and Bretherton 2014; Merlis et al. 2016; Chavas and Reed 2019; Hsieh et al. 2020; Stansfield and Reed 2021). The β-plane has been used in several recent studies considering TC genesis and behavior (Fedorov et al. 2018; Fu et al. 2019, 2021; Bercos-Hickey and Patricola 2021; Vu et al. 2021). However, process-oriented diagnostics of latitudinally-varying modes of organized convection have been primarily limited to GCMs, which are limited by relatively coarse resolution and the necessity to employ a convective parameterization. With computational advances, global or near-global cloud resolving model (CRM) simulations have become feasible (Satoh et al. 2019), but are quite computationally expensive to run on the time scales needed to simulate RCE.

In this manuscript, convection-permitting β-plane simulations test the findings of CW20 and CW22 in a more realistic setting. The model configuration is designed to accommodate multiple modes of organized convection without the need for a cumulus parameterization, over a sufficient time to reach an equilibrium state. In reality, β varies with the cosine of the latitude, approaching zero near the poles and becoming dynamically equivalent to an f-plane at high latitudes (Chavas and Reed 2019). Here, β is held constant in each simulation, such that f varies linearly in a Cartesian grid. The overarching goal is to understand fundamental modes and mechanisms of SA as a function of background rotation (represented by f and β), absent other influences. We center our discussion around three key questions. First, how do the mechanisms contributing to SA onset and maintenance change as a function of f, and where does aggregation onset occur most quickly? Second, how does equilibrium TC activity vary as a function of both f and β, including genesis, intensity, and density? Finally, what are the dominant modes of SA at low latitudes when β is introduced, and how do they evolve from the spinup to equilibrium periods? Information about the model and simulation design is provided in Section 2. Section 3 describes the SA process using diagnostics such as the frozen moist static energy (FMSE) variance budget of Wing and Emanuel (2014). Specific high-latitude and low-latitude modes of organized convection are discussed in greater detail in Sections 4 and 5, respectively. Section 6 discusses how the results presented in this work compare to those from similar model configurations in the prior literature. Finally, conclusions and future research priorities are presented in Section 7.

2. Simulation Design

Five 100-day β-plane simulations are developed using the System for Atmospheric Modeling (SAM) version 6.11.2 (Khairoutdinov and Randall 2003), which employs the anelastic equations of motion. The prognostic thermodynamic variables are total non-precipitating water, total precipitating water, and liquid water/ice static energy. A square domain spans 10240 km in each horizontal dimension, analogous to roughly 90° of latitude on Earth and 6.7 times larger in each dimension than the f-plane simulations in CW20 and CW22. Simulations are run with explicit convection (5 km horizontal grid spacing) on an Arakawa-C grid. The lowest vertical level is at 37 m, and a stretched vertical grid is used with 75 m grid spacing near the surface, expanding to 500 m above 3.5 km. There are 74 vertical levels up to the model top at 33 km, with Newtonian damping applied in a sponge layer spanning the upper third of the domain. The east and west boundaries are periodic, but the incorporation of β here necessitates rigid walls along the north and south boundaries.

There is uniform thermal forcing following the RCEMIP protocol (Wing et al. 2018), with constant 300 K SST and insolation of 413 W m^{-2} (corresponding to the tropical annual mean with a solar constant of 650.83 W m^{-2} and a zenith angle of 50.5°). The model schemes are the Rapid Radiative Transfer Model for radiation (Clough et al. 2005; Iacono et al. 2008; Mlawer et al. 1997), a Smagorinsky-type parameterization for subgrid-scale fluxes, and SAM's default one-moment microphysics. The initial sounding is an equilibrium sounding from the 300 K non-rotating small-domain SAM simulation in RCEMIP (Wing et al. 2020). Motion and convection are initialized by random temperature perturbations of 0.1 K in the lowest level, reducing linearly to 0.02 K at the fifth vertical level. These settings are largely kept identical to those in the prior f-plane simulations in CW20 and CW22, in order to better constrain the role of varying f in a single domain. At the same time, the favorable conditions for TCs under higher f here (sufficiently warm SST, no prescribed vertical wind shear, strong planetary vorticity) yield a large sample of TCs to study with convection-permitting resolutions. This provides a more realistic analog to "TC World" simulations (Khairoutdinov and Emanuel 2013; Cronin and Chavas 2019), which increase f by an order of magnitude above normal tropical values to accommodate numerous small TCs in a small domain. We also produce a convection-permitting counterpart to aquaplanet GCM simulations that employ uniform thermal forcing (Shi and Bretherton 2014; Merlis et al. 2016; Chavas and Reed 2019), which can be used to evaluate the importance of resolution and explicit convection on the depiction of TCs in this environment.

We refer to f via the effective latitude, or the latitude on the real Earth corresponding to a given value of f. Three simulations are centered on 15°N (Table 1). One employs an approximate real-Earth mid-latitude (51°N) value of β (FULL15), another reduces this value to capture half of the effective latitudinal range (HALF15), and the third enhances that range by a factor of 1.5 (ENHD15). Reducing β increases the area between effective latitudes relative to FULL15, and vice versa. These three simulations assess how the magnitude of β influences the time scales, relevant processes, and resulting modes of convective organization, as well as TC characteristics such as frequency and intensity. The range of effective latitudes covered by each of these simulations includes both an equator and at least subtropical latitudes where numerous TCs are expected. Two additional simulations employ the "full" value of β, but are centered at 0° (FULL00) and 45°N (FULL45). FULL00 is designed to assess near-equatorial convection with minimal influence by the rigid meridional boundaries, while FULL45 targets high-latitude cyclone activity.

TABLE 1. Full list of β-plane simulations developed for this study, with domain settings. The first three test the sensitivity of SA to the magnitude of β, while the latter two target low-latitude and high-latitude modes with minimal influence from the rigid meridional walls. All simulations are the same physical size - a 10240 km square.

Simulation Name	Center Effective Latitude	Effective Latitude Range	Range of f (s^{-1})	Value of β (s^{-1} m^{-1})
FULL15	15°N	30°S-60°N	-7.29×10^{-5}-1.26×10^{-4}	1.43×10^{-11}
HALF15	15°N	7.5°S-37.5°N	-1.90×10^{-5}-8.88×10^{-5}	1.05×10^{-11}
ENHD15	15°N	52.5°S-82.5°N	-1.16×10^{-4}-1.45×10^{-4}	2.55×10^{-11}
FULL45	45°N	0°-90°N	0-1.46×10^{-4}	1.43×10^{-11}
FULL00	0°	45°S-45°N	-1.03×10^{-4}-1.03×10^{-4}	1.43×10^{-11}

3. Regimes of Self-Aggregation

a. Spatial and Temporal Evolution of Convection

The spatial distribution of column relative humidity is shown for the first 40 days of FULL15 in Figure 1, noting that all simulations behave qualitatively similarly (Movie S1-S5). Dry patches are initially prominent at low latitudes, consistent with non-rotating and "low-f" SA as in CW22 (Figure 1a). Several TCs then spin up near the meridional boundaries, where f is highest (Figure 1b). Thereafter, TCs form intermittently at lower latitudes, but generally remain poleward of 10°. By day 20, two distinct latitudinal regimes of organized convection are apparent. The low-latitude regime is mostly characterized by eastward-propagating equatorial waves. The high-latitude regime exclusively features TCs, which tend to intensify into hurricanes unless interfered with by other nearby systems or the meridional walls. As in CW22, intense TCs dry their surrounding environments (Figure 1c-d). Between days 30-50 in the low-latitude belt, convectively-coupled waves are less apparent, masked by deep-layer easterly flow. This marks a transition period between the simulation's spinup stage, which encompasses the onset of SA, to the eventual equilibrium stage over the final 40 days. These three stages will be discussed further in Sections 4-5.

Given these two regimes of SA, it is appropriate to examine various thermodynamic and dynamic fields as a function of the effective latitude. This includes FMSE and its spatial variance, where FMSE is given by the sum of contributions from temperature (c_pT), gravitational potential energy (gz), and latent processes from water vapor and ice (L_vq_v and L_fq_{ice}):

$$h = c_pT + gz + L_vq_v - L_fq_{ice} \tag{1}$$

Figure 2 presents time series of column precipitable water (PW), outgoing longwave radiation (OLR), FMSE variance, and 500 hPa subsidence fraction (SF) in FULL15. All are averaged in 10° latitudinal bins (averaged between hemispheres), as well as broader "TC" and "EQ" belts. These are simply the areas occupied and not occupied by TCs, respectively, separated by the minimum latitude where a tropical storm center is identified (wind speed ≥ 18 m s^{-1}, tracking algorithm described in Section 4) in each simulation. All grid points "equatorward" of this latitude are assigned to the EQ belt, while "poleward" grid points are assigned to the TC belt (Table 2)

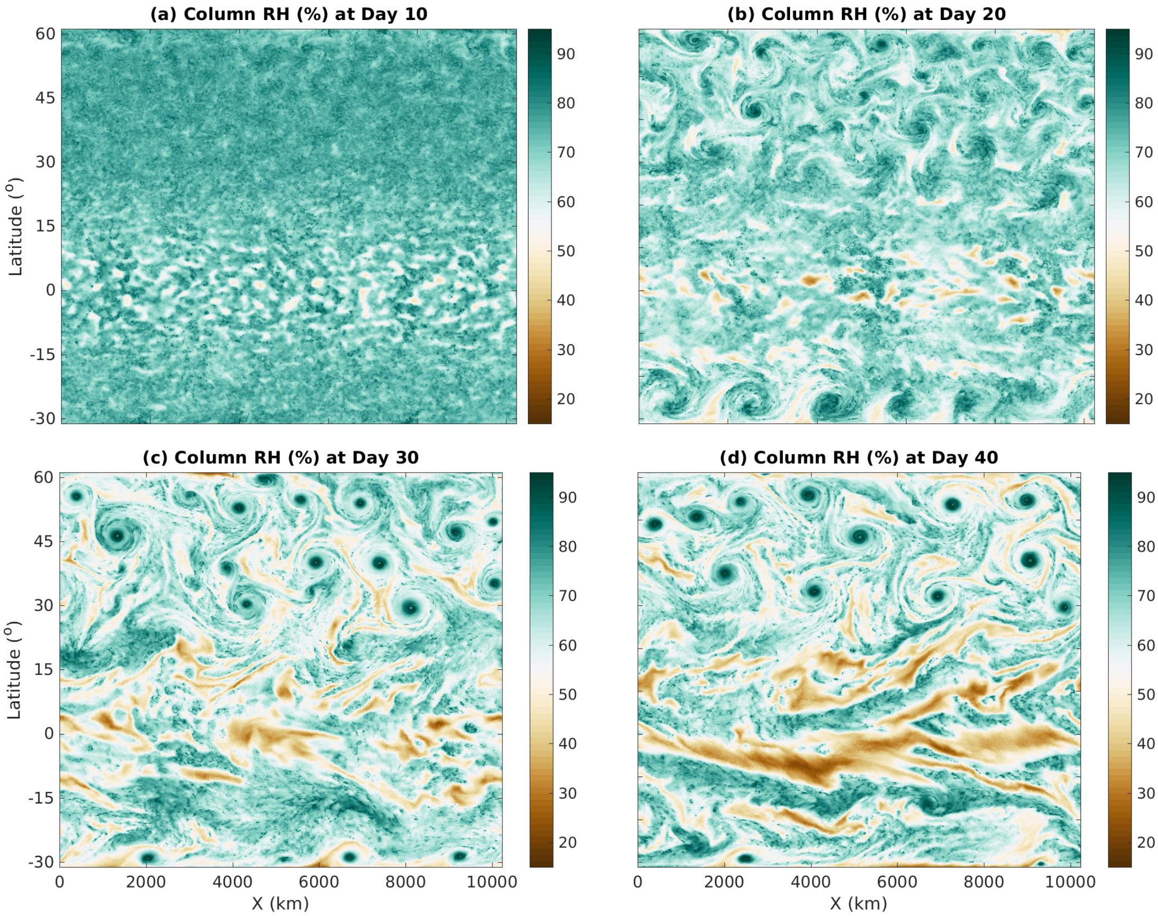

Fig. 1. Spatial distribution of column relative humidity in FULL15, at (a) day 10; (b) day 20; (c) day 30; (d) day 40. The effective latitude is plotted on the y-axis. In this case, the equator ($f = 0$) is near Y = 3500 km.

to simplify comparison of the two regimes. The dividing latitude in FULL15 is 13.99°. SF is calculated using 500 hPa vertical velocity averaged daily in 80 km square blocks. This smooths out the effects of individual updrafts, and better captures an aggregated state over large space and time scales.

SA is associated with high OLR, FMSE variance, and SF, and with lower PW - a drier mean state with more large-scale subsidence and more separation between dry and moist air, regardless of the exact mode of the aggregated convection. Steady drying (reduction of PW) takes place over the first 20 days, shown for FULL15 in Figure 2a. This occurs more quickly at low latitudes, implied by the separation between the TC and EQ curves shortly after initialization. The differing behavior of the TC and EQ belts implies important differences in the time scales and dominant

TABLE 2. Range of latitudes (absolute value) covered by the TC and EQ belts in each simulation. The boundary between the belts is the minimum latitude at which a tropical storm (wind speed ≥ 18 m s^{-1}) is identified via the tracking algorithm described in Section 4.

Simulation Name	EQ Belt	TC Belt
FULL15	0°-13.99°	13.99°-60°
HALF15	0°-9.00°	9.00°-37.5°
ENHD15	0°-12.60°	12.60°-82.5°
FULL45	0°-17.46°	17.46°-90°
FULL00	0°-17.09°	17.09°-45°

processes behind SA onset, even during the model's spinup. Drying takes place with time at all latitudes, but mean PW increases with latitude, reflecting the increasing prevalence of TCs as a particularly moist mode of aggregated convection. Though noisier, OLR (Figure 2b) displays a similar evolution. Notably, OLR increases in the TC belt initially lag those of lower latitudes, but catch up rapidly from day 20-40. This is concurrent with the development of TCs as a rotating mode of self-aggregated convection. A lag between the initial genesis and the OLR increase exists because significant cloud cover reduction takes place after the TCs intensify.

The FMSE variance time series (Figure 2c) elegantly depicts the separation of the two regimes within the first 10 days, followed by the recovery of the TC belt to a "more aggregated" state by day 20. In the first 10 days, high FMSE variance at low latitudes reflects the preferential growth of dry patches near the equator. Beyond 20°, the initial separation of dry and moist patches is stunted as FMSE variance briefly decreases, and does not recover substantially until widespread TC activity begins. By day 100, FMSE variance is highest near the meridional walls, consistent across all simulations. The subsidence fraction (Figure 2d) oscillates between 0.65-0.85 and increases markedly during the spinup period over the first 30 days, which indicates that the majority of the domain is under large-scale subsidence. The first 20 days again suggest that the onset of SA occurs more quickly at low latitudes, as the subsidence fraction in the EQ belt is higher. Like the other thermodynamic parameters, the TC belt catches up by day 20. The SA onset process is consistent across all simulations, with the only difference being in the time scale of the initial TC spinup (Movie S1-S5). This difference is small (less than 10 days), where TC genesis occurs more quickly

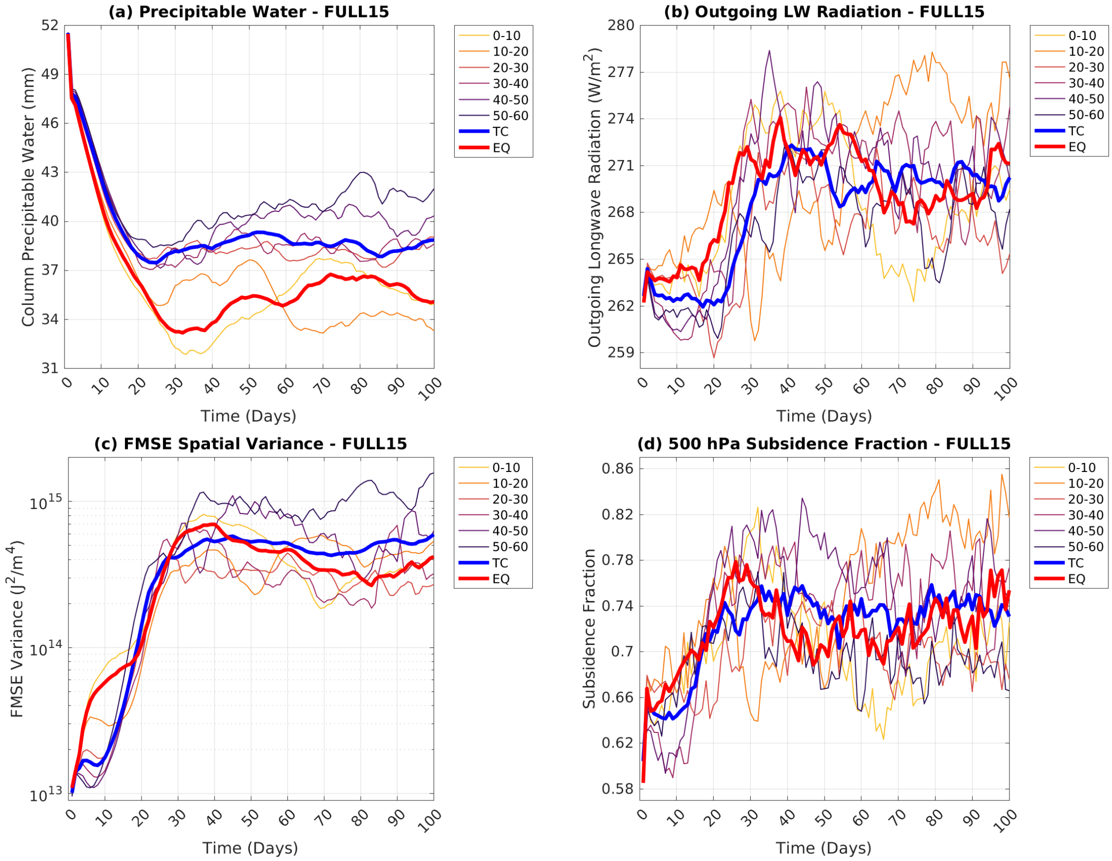

FIG. 2. Time series of (a) precipitable water, (b) outgoing longwave radiation, (c) FMSE variance, and (d) subsidence fraction, averaged in 10° latitudinal bins in the FULL15 simulation. TC and EQ belts are separated by the minimum latitude of tropical storm occurrence (Table 2). Data are averaged daily, while subsidence fraction is calculated using vertical velocity averaged in (80 km)^2 blocks to characterize the large-scale motion.

for simulations that feature higher values of f at the boundaries, to be discussed further in Section 4.

b. FMSE Variance Budget

Feedbacks contributing to SA are quantified with the FMSE spatial variance budget given by Eq. 2 (Wing and Emanuel 2014), capturing processes influencing the separation of dry and moist air under uniform thermal forcing. Positive feedbacks occur where anomalies of FMSE and the other variables in Eq. 1 (surface enthalpy flux, radiative flux convergence, etc.) match sign.

$$\frac{1}{2}\frac{\partial \hat{h}'^2}{\partial t} = \hat{h}'SEF' + \hat{h}'NetSW' + \hat{h}'NetLW' - \hat{h}'\nabla_h \cdot \widehat{\vec{u}h} \tag{2}$$

Primes denote anomalies from the domain mean, and hats indicate mass-weighted vertical integrals. The first term on the right-hand side is the surface flux feedback, a correlation of the anomalies of FMSE and the surface enthalpy flux, the sum of latent and sensible heat fluxes. The second and third terms are the radiative feedbacks, correlating anomalies of FMSE and column shortwave and longwave flux convergence, respectively. The combined effects of radiative and surface enthalpy fluxes make up the total feedback from diabatic processes. The final term is the advective feedback, representing the column flux divergence of FMSE due to circulations. This is often calculated as a residual, but is done explicitly here by diagnosing the tendency of FMSE due to advection online as the model is running.

To break down the specific physics behind the feedbacks and their latitudinal variability, Figure 3 shows the composite mean feedbacks across all simulations, averaged daily. Time series of the full feedbacks (similar to Figure 3a) are shown in Figure S1b-f in the Supporting Information for individual simulations, to demonstrate the approximate collapse to a dependence on *f*. The same conventions for the TC and EQ belts in Table 2 are employed here, and the spinup period is again included to highlight processes behind SA onset. Longwave and shortwave feedbacks can be decomposed into cloud and clear-sky contributions, while the surface flux feedback is composed of wind speed, air-sea enthalpy disequilibrium, and eddy terms. The wind speed contribution is essentially a wind-induced surface heat exchange (WISHE) feedback on moisture anomalies (Emanuel 1986). The surface flux feedback is the strongest positive feedback at high latitudes due to the co-location of strong winds and ample moisture in the TC circulation (Figure 3a). In the EQ belt, the surface flux feedback is initially strongly positive, then becomes weak or negative after day 30. Following a gradual increase early on, the shortwave feedback exhibits little temporal variability, and is stronger at low latitudes - the strongest positive feedback there after day 40. The longwave feedback is positive at high latitudes, but becomes negative or near zero farther equatorward by day 30. The advective feedback is negative throughout the simulations after initialization, but it is much more strongly negative at high latitudes, consistent with f-plane simulations in CW22.

Cloud-longwave radiative effects are positive contributors to FMSE variance as deep convective clouds enhance longwave radiative heating, increasing the FMSE of regions that are already moist (Figure 3b). This feedback is most pronounced at high latitudes, a process that also feeds back on TC intensity (Ruppert et al. 2020; Wing 2022). In dry areas with large-scale subsidence, low clouds enhance radiative cooling. In contrast, the clear-sky longwave feedback is negative throughout the domain after the first 20 days, cancelling or even overcompensating the positive cloud-longwave feedback at low latitudes. This negative feedback stems from increased longwave emissivity in regions with anomalously high FMSE, which increase OLR (Wing and Emanuel 2014). The negative longwave feedback in the EQ belt is strongest from days 30-50.

In contrast, clear-sky effects dominate the shortwave feedback after the first 15 days (Figure 3c), though the cloud shortwave feedback is also weakly positive. This is primarily due to absorption of solar radiation by water vapor, causing greater shortwave heating in areas with high FMSE. This becomes the strongest positive feedback in the EQ belt, while at higher latitudes it is weaker than the longwave and surface flux feedbacks. The wind speed term is the positive contributor to the surface flux feedback throughout the domain (Figure 3d), particularly at high latitudes in the strong winds of the TCs. At low latitudes, enhanced surface fluxes still result from convective gustiness. There, however, the positive wind speed feedback is later offset by a negative air-sea enthalpy disequilibrium feedback. This is because dry regions feature stronger disequilibrium between the ocean surface and atmosphere, which would amplify surface fluxes for the same wind speed, and vice versa for moist regions. Amplified surface fluxes in a dry region, or dampened surface fluxes in a moist region, would counteract existing FMSE anomalies and result in a negative feedback on FMSE variance.

While the modes of organized convection differ under weak rotation in f-plane (CW22) and β-plane simulations (isolated bands or circular clusters versus convectively-coupled waves), the separation of SA into two well-defined regimes as a function of f in these β-plane simulations is consistent with CW22. This can also be seen in Figure 3e-f, which show the overall and decomposed feedbacks composited across the final 40 days of all simulations as a continuous function of latitude, exhibiting a qualitatively similar dependence as in CW22. At low latitudes,

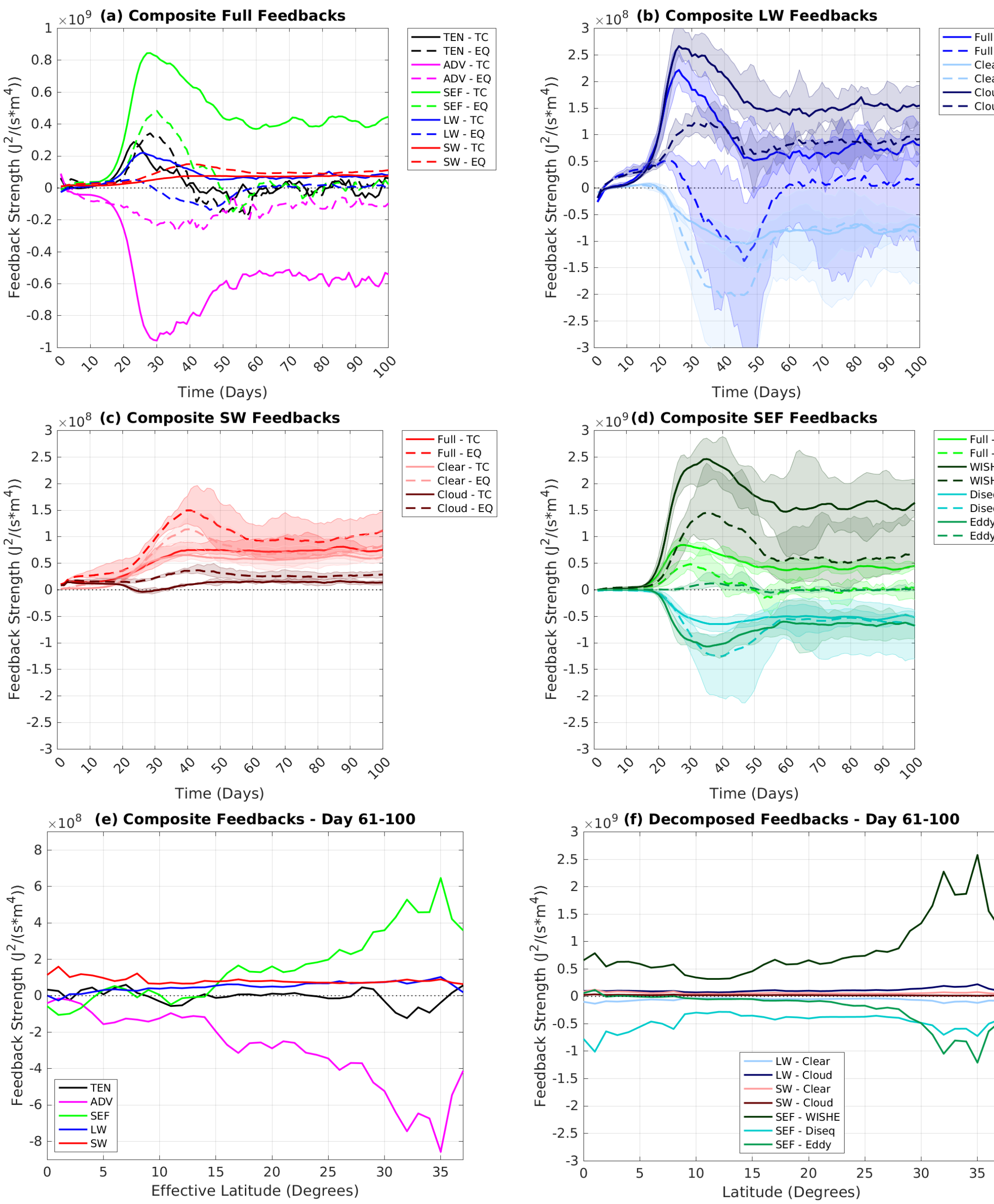

FIG. 3. (a-d) Composite time series of FMSE variance budget feedbacks across all simulations, including (a) overall feedbacks and decomposed (b) longwave, (c) shortwave, and (d) surface enthalpy flux feedbacks. Values are averaged daily in the TC (solid) and EQ (dashed) belts, as identified in Table 2. Shaded in (b-d) are the ranges of each decomposed feedback across the simulations at each day. (e-f) Composited feedbacks as a continuous function of latitude, averaged across the final 40 days of each simulation.

radiative and surface flux feedbacks drive SA onset, while shortwave clear-sky effects maintain the aggregated state in the equilibrium stage (Figure 3e). Convection does not organize as easily at higher latitudes early on, but the stronger background rotation permits TC genesis. The TCs drive further aggregation via strong WISHE and cloud-longwave feedbacks (Figure 3f). Each of these processes competes with an advective feedback that is the leading-order negative term at all latitudes, but becomes more strongly negative as f increases. With the regimes of SA highlighted, the next two sections will more closely examine the statistics, structure, and evolution of TCs and equatorial waves.

4. Tropical Cyclones

Given the favorable environmental conditions, TCs persist for tens of days unless interfered with by other TCs or the meridional boundaries. Candidates are first identified using the 850 hPa relative vorticity field. Every six hours, the average relative vorticity is computed within a 150 km box surrounding each grid point. From this smoothed field, local maxima of at least 10^{-4} s^{-1} that persist for 2.5 days are retained as disturbances. This threshold for relative vorticity is slightly lower than that used by Zhang et al. (2021) and Hsieh et al. (2020) for identifying seeds from an unsmoothed vorticity field in a GCM. Several thresholds were tested to optimize the algorithm, with the goal of capturing genesis events with multiple days of lead time. Lower thresholds of relative vorticity identified disproportionally more non-developing disturbances and converged to a similar number of developing disturbances. Meanwhile, higher thresholds failed to capture many genesis events with satisfactory lead time, or failed to identify some weak tropical storms at all. TC genesis is defined as the first time that a disturbance achieves a maximum near-surface wind speed of 18 m s^{-1} (tropical storm intensity), then persists for at least one day. We note that several different definitions of genesis have been used in prior literature, which may influence results. To test this possible sensitivity with a recent example, we also computed our genesis statistics with the method employed by Chavas and Reed (2019), using local pressure minima with a closed contour of at least 4 hPa below the surrounding environment within a 550 km circle. Our results were not significantly altered.

The tracking algorithm searches for one local maximum of relative vorticity (disturbance) within a 550 km search radius (approximately 5°). There are two instances when a disturbance may be dropped by the algorithm as a result: if its center is within 550 km of a meridional boundary, or if two disturbances are within 550 km of each other such that only the stronger of the two is retained. Disturbances initialized with wind speeds above 20 m s^{-1} are assumed to re-emerge from one of these conditions, and are removed from genesis analyses. Future work may revise the tracking algorithm to permit the study of Fujiwhara-type interactions in this model configuration. Across the five simulations, the number of "repeat" genesis events ranges from 7 to 42.

a. Tropical Cyclone Statistics

After filtering, the cumulative number of disturbances (distinct vorticity maxima meeting the 10^{-4} s^{-1} threshold) ranges from 42 (HALF15) to 132 (ENHD15) across the full 100 days of a given simulation (Figure 4a). About 50% of these disturbances achieve the genesis definition to become tropical storms, and about 40% of the total disturbances become hurricanes with wind speeds exceeding 33 m s^{-1}, where the dashed lines in Figure 4a accumulate at the time a disturbance first reaches hurricane intensity. ENHD15 develops the most hurricanes, followed by FULL45, FULL15, FULL00, and HALF15. FULL45 and ENHD15 (the simulations capturing the highest latitudes) develop disturbances the earliest, followed by FULL15 (maximum latitude of 60°), then FULL00 (45°), then HALF15 (37.5°).

Figure 4b-c shows the latitudinal and temporal distribution of genesis events using our persistent 18 m s^{-1} near-surface wind speed threshold, and the genesis rate calculated using a 10-day centered running mean. The genesis rate is maximized from day 15-25 as the initial spinup takes place preferentially near the boundaries (Figure 4c). This is most amplified in ENHD15 and FULL45, suggesting that the upper limits of f in the domain most strongly control the frequency of initial genesis events. Equatorward of 35° (near the latitudinal extent of HALF15), there is little systematic variation in genesis rate with β (not shown). Therefore, the amplified genesis rate in ENHD15 and FULL45 is due to a combination of stronger maximum f (as in Chavas and Reed (2019) and CW20), and a larger area with high f. This is magnified further by the Cartesian domain geometry, which provides a larger surface area for high-latitude TCs relative to spherical geometry. The genesis rate is lowest from days 30-60 (Figure 4c), and there are no genesis events beyond 40° from days 38-60, even for ENHD15 and FULL45 (Figure 4b). This abrupt shift in genesis behavior signals the start of the transition period between the spinup and equilibrium stages, which also corresponds

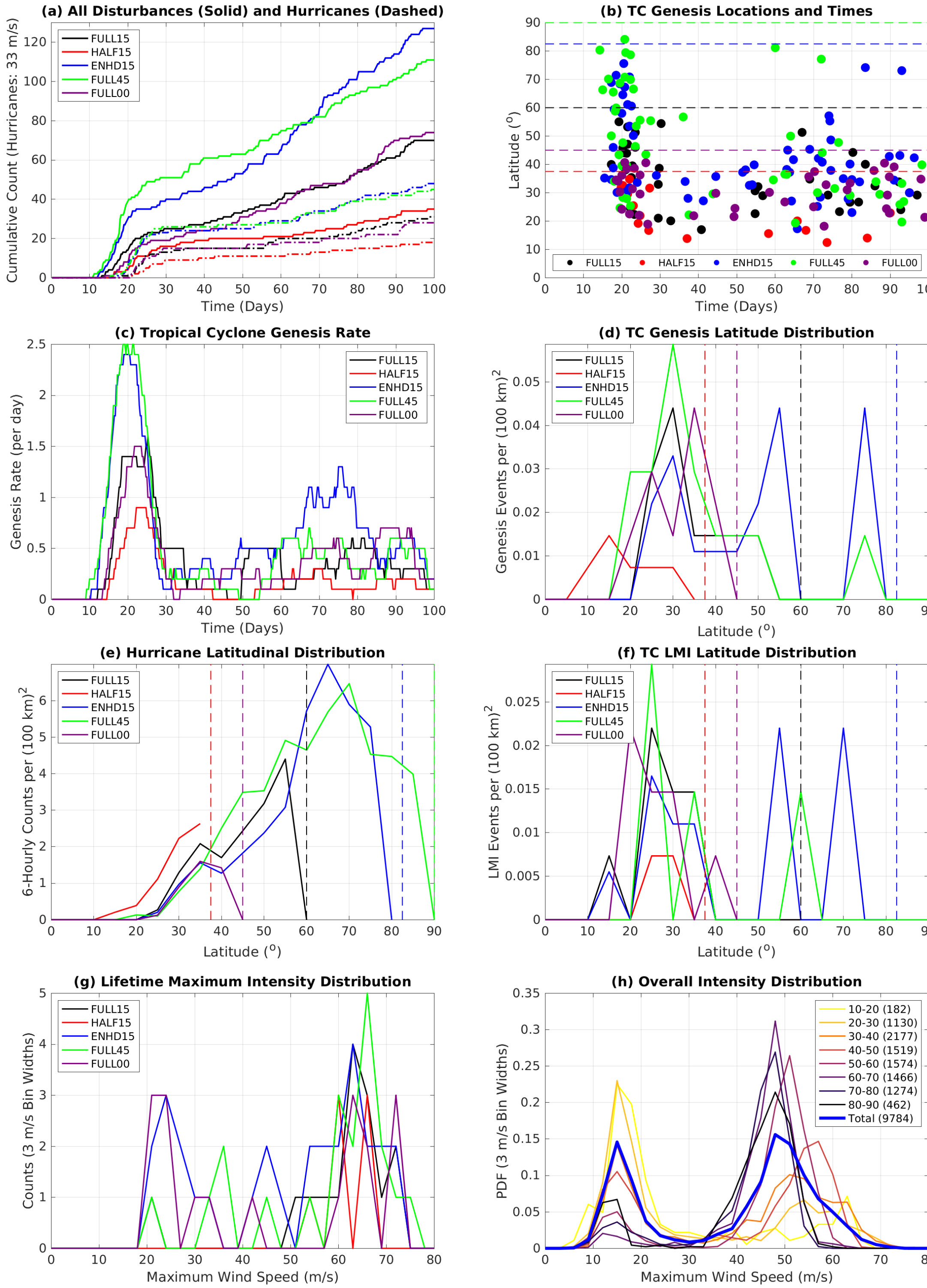

FIG. 4. (a) Accumulated disturbance and hurricane counts; (b) times and latitudes of individual genesis events; (c) genesis rate using a 10 day running mean; (d-f) latitudinal distribution of hurricane track density, TC genesis, and lifetime maximum intensity per (100 km)^2 in 5° bins; (g) distribution of LMI wind speeds in 3 m s^{-1} bins; (h) intensity distribution of all TC snapshots organized by latitude. (d-h) only use TCs over the final 40 days of each simulation. Dashed lines in (b) and (d-f) represent the upper latitude bounds in each simulation.

to a damping of low-latitude wave activity to be discussed in the next section. ENHD15 generally produces the highest average genesis rate from day 40-85 - about one new tropical storm daily.

To compare latitudinal genesis, track, and intensity distributions of simulations with different magnitudes of β, the counts at each latitude are normalized by area before being placed into 5°-wide latitude bins. This accounts for HALF15 having a larger area between effective latitudes than the other simulations, for instance. For the ensuing analyses shown in Figure 4d-h, only TCs (tropical storms and hurricanes) after day 60 are considered to better reflect the equilibrium state of the simulations. As suggested by Figure 4b, the equilibrium genesis distribution mostly peaks in the subtropical latitudes. While this peak is subtle and genesis occurs at a wide range of latitudes in each simulation, each has its peak between 25-40° except for ENHD15. This includes FULL15 and FULL45, which have substantial surface area at higher latitudes to accommodate genesis events.

At equilibrium, hurricanes (wind speeds ≥ 33 m s^{-1}) tend to co-exist at high latitudes, including those that originate at lower latitudes and propagate via the β-drift mechanism (Holland 1983). Accordingly, hurricane track density is found to generally increase with latitude (Figure 4e). There is a robust peak at the highest latitudes in each simulation (Figure 4e). The minimum latitude that a hurricane (tropical storm) is identified at in HALF15 is 11.66° (9°). ENHD15 has no hurricanes equatorward of 24.63°, suggesting that the value of β affects the latitudinal reach of the equatorial wave regime. With the exception of HALF15, the minimum latitudes of hurricanes and tropical storms are 19.66° and 12.60°, respectively. In other words, the "low-f" (effective latitudes < 8°) TC genesis in the f-plane simulations of CW20 and CW22 does not occur here.

Figure 4f displays the latitudinal distribution of the lifetime maximum intensity (LMI) for all tropical storms and hurricanes. The most prevalent feature is again a modest peak between 20-40°, which again occurs in all simulations except for ENHD15. LMI also often occurs at higher latitudes in each simulation. Combined with the hurricane density statistics in Figure 4e, this implies that TCs can reach peak intensities at high latitudes, but the optimal environment for maximizing intensity is farther equatorward with less surrounding TCs to destructively interact with.

The distribution of LMI itself is shown for all tropical storms and hurricanes in Figure 4g. This is a bimodal distribution showing a cluster of weak tropical storms with winds near 20 m s^{-1}, and a primary peak of 60-75 m s^{-1} major hurricanes. The latter is expected given the extremely favorable environment, which provides numerous cases of rapid intensification that can be examined in future work. The subset of weak tropical storms and non-developing vorticity maxima is useful to identify predictors for genesis and intensification using a composite approach, which will be performed in the next subsection.

The overall intensity including all disturbances also follows a bimodal distribution (Figure 4h, with peaks near 15 m s^{-1} (below tropical storm strength) and 50 m s^{-1} (Category 3 hurricanes). Systems which do develop tend to intensify quickly, limiting the sample of strong tropical storms and marginal hurricanes. The peak TC intensity across all simulations is near 75 m s^{-1}. This is near the theoretical potential intensity (Emanuel 1986), which lies between 70-80 m s^{-1} when computed from the domain-mean sounding at each hour. Thinner lines on Figure 4h decompose the TC intensity distribution into 10° latitudinal bins. From 10-20° (yellow line), the distribution is skewed toward the weakest intensities as disturbances rarely intensify into hurricanes equatorward of 20°. As the effective latitude increases, the proportion of weak TCs decreases while that of hurricanes increases. At higher latitudes, the peak intensity shifts towards lower intensities. This reflects the growing impact of multi-TC interactions, given the increased density of TCs at high latitudes in this model configuration (Figure 4e). Like the LMI latitudinal distribution, this implies that TCs are usually strongest at intermediate latitudes when there is more separation between them.

b. Genesis Processes

Developing and non-developing disturbances are next composited across all simulations to highlight important contributors to TC genesis (Figure 5). Figure 4g revealed a bimodal distribution of lifetime maximum intensities, indicating that the vast majority of disturbances which successfully strengthened beyond minimal tropical storm intensity would subsequently intensify further into major hurricanes. To clearly demarcate these two groups in this analysis, we identify developing disturbances as those first identified with wind speeds under 18 m s^{-1} that later intensify into hurricanes ($\geq$ 33 m s^{-1}), while those which do not achieve the 18 m s^{-1} wind speed threshold for at least one full day consecutively are considered non-developing. This comparison is limited to the TC belt, defined for each simulation in Table 2, which excludes some non-developing disturbances that are identified farther equatorward. Moreover, only disturbances after day 60 are considered to reflect the equilibrium state of the simulations. Vertical profiles considered include cyclonic relative vorticity, relative humidity, anomalies of virtual temperature and longwave heating rate (from the mean of an 1100 km TC-centered box), and cloud condensate, plotted as the difference between the developing and non-developing composites. These quantities are averaged at each vertical level from 0-12 km in a 300 km box centered on the disturbance, and composited by the maximum wind speed of the disturbance up to 18 m s^{-1}. With the exception of the 10-11 m s^{-1} bin for developing disturbances, each composite includes no less than 20 snapshots (Figure 5a).

Developing TCs have higher initial relative vorticity throughout the lower and middle troposphere than non-developing cases (Figure 5a). The radial and vertical distributions of relative vorticity vary widely across developing cases, with no clear systematic dependence on latitude within the broader TC belt prescribed in Table 2. The altitude of the initial vorticity maximum preceding TC genesis ranges from 1.5-6 km, a wider range than in the f-plane simulations in CW20, but still consistent with the top-down "high-*f*" genesis pathway described in CW20. Recall that no TCs form equatorward of 9° in these simulations. Accordingly, there is no evidence of "bottom-up" TC development throughout the individual cases. The importance of amplified mid-tropospheric vorticity in the developmental stages is clear from Figure 5a, as large differences between the developing and non-developing composites extend well into the mid-troposphere.

Moisture profiles also serve as a useful predictor for TC development in these simulations (Figure 5b). There is little difference in the boundary layer relative humidity (RH), which typically exceeds 80%. However, developing cases have a moister free troposphere, with RH values about 10-15% higher from 3-7 km in developing disturbances at low wind speeds (i.e. the earliest stages of development). This is in alignment with observations, where the mid-tropospheric relative humidity is considered a useful indicator of genesis potential (Emanuel and Nolan 2004; Hopsch et al. 2010). This is because moist mid-levels prevent dry air entrainment and favor more persistent convection with weaker downdrafts, limiting import of low-entropy air into the boundary layer (Tang and Emanuel 2012). While the difference in RH between developers and non-developers reduces as winds approach 18 m s^{-1}, developing cases are still about 5% moister in mid-levels at the tropical storm wind threshold. Consistent with the amplified moisture, developing TCs also exhibit more amplified virtual temperature anomalies aloft (Figure 5c). The difference between developing and non-developing cases is greatest in the middle and upper troposphere, resembling the characteristic warm core TC structure aloft.

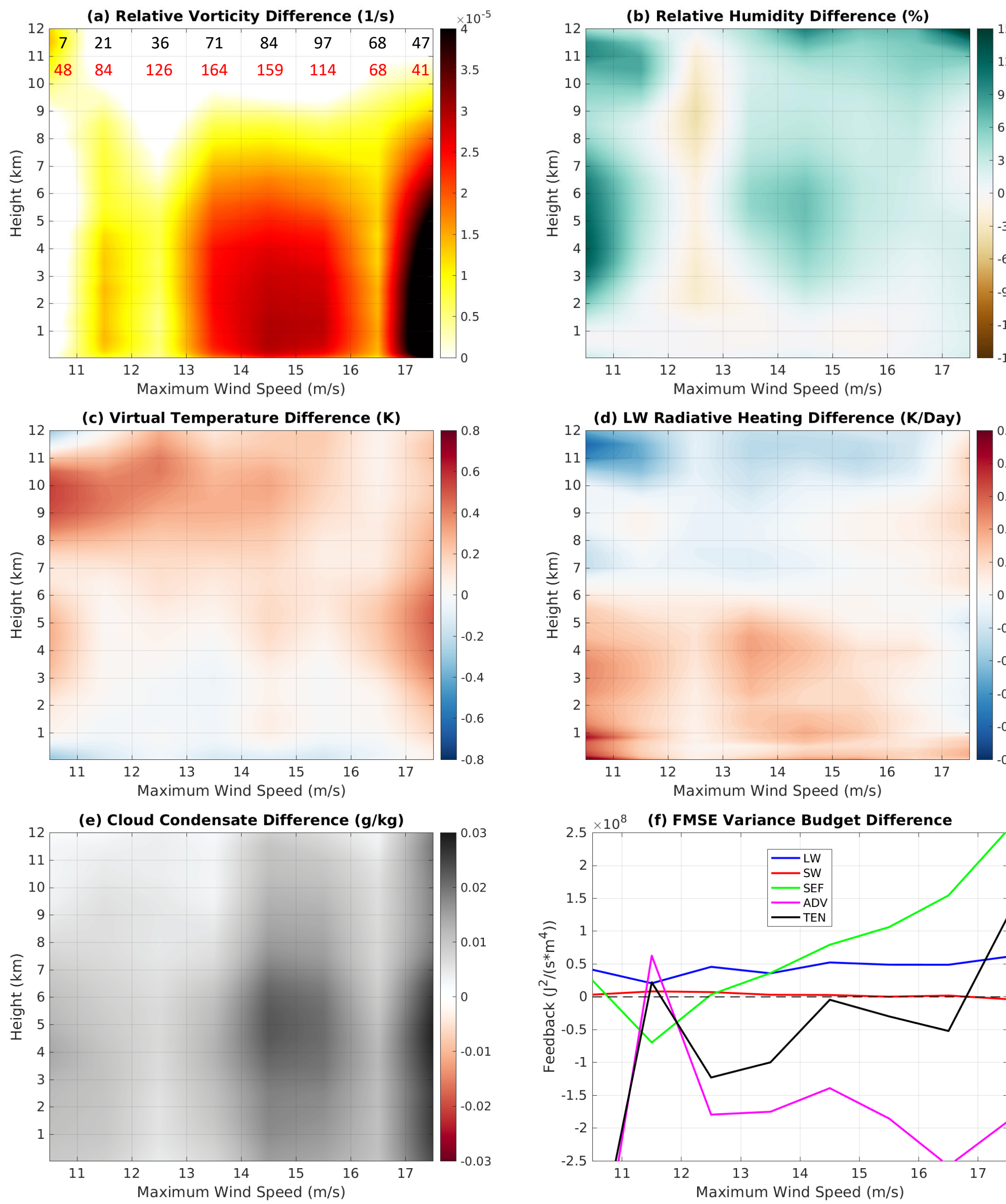

FIG. 5. Differences between developing and non-developing TCs, composited across all simulations by the maximum wind speed of the disturbance. Developing TCs are those which intensify into hurricanes, while non-developing disturbances fail to maintain 18 m s^{-1} wind for at least one day. (a-e) show vertical profiles of (a) relative vorticity; (b) relative humidity; (c) virtual temperature anomaly; (d) longwave heating rate anomaly; (e) cloud condensate. (f) displays the FMSE variance budget feedbacks. Sample sizes for each wind speed bin are shown in (a) for the developing (black) and non-developing (red) groups.

Examination of cloud profiles reveals that developing cases, as expected, feature more deep convection that contributes to the anomalous warmth aloft via latent heat release and enhanced radiative heating (Figure 5d-e). Longwave heating is enhanced below 7 km in the earliest stages of development, and as the wind speed increases above 15 m $^{-1}$, the column of stronger longwave heating shifts upward (Figure 5d). This suggests that enhanced deep convective cloud coverage feeds back positively on TC development (Ruppert et al. 2020). Indeed, developing TCs have higher cloud condensate throughout the column, with the difference between developing and non-developing cases growing with wind speed (Figure 5e). The difference extends above the freezing level (about 5 km), suggesting that ice processes and high clouds are influential in the development stage (Wing 2022). Figure 5f confirms that the longwave radiative feedback on FMSE variance is larger in developing systems than non-developers, and this difference grows with wind speed. This is accompanied by an even larger difference in the strength of the surface flux feedback in developers, which eventually compensates for a more strongly negative advective feedback. The difference in the longwave and surface flux feedbacks between the developing and non-developing composites is on the order of 50% of the equilibrium average value of the feedbacks in the broader TC belt.

5. Equatorial Waves

Analysis of convectively-coupled equatorial wave (CCEW) activity primarily considers the FULL00 simulation, centered on the equator. Simulations behave qualitatively similarly, with the exception of the time scales of wave growth and damping to be discussed via Figure 6f. Figure 6a-b reveals the development and zonal propagation of CCEWs, identified by fields of 500 hPa vertical velocity and 200 hPa zonal wind with precipitation rate overlaid. At each zonal grid point, these quantities are averaged six-hourly from 7.5°S-7.5°N to avoid influences from TCs, as no strong TCs exist equatorward of 10°. After a short initialization period over the first 5 days, eastward-propagating oscillations become readily apparent corresponding to convectively active and suppressed wave phases. Ascent, upper-level zonal divergence, and amplified precipitation are in phase with one another (red shading and green contours in Figure 6a, transition from orange to purple shading in Figure 6b). The phase speed of these eastward-propagating waves is estimated to be near 15 m s^{-1} during both the first 30 days and the final 30 days, within the range of observed

Kelvin wave phase speeds (Baranowski et al. 2016). There are typically three convectively active wave phases at a given time, implying an average separation distance of 3000-4000 km.

The pattern dominated by these disturbances exists through the spinup period of each simulation, with the only difference being that waves emerge more quickly when β is amplified. Some evidence of westward-propagating disturbances is also apparent in Figure 6a-b, though these are less pronounced and less influential on the overall convective distribution. After day 30, however, the equatorial regime transitions to one dominated by easterly winds (Figure 6b). During this time, enhanced variability in meridional winds implies that there is more interaction between the TC and EQ belts (Figure 6c), given that TCs have developed and matured by this point. In the second half of the simulation, waves appear prominently again in Figure 6a-b, and the upper-level meridional winds relax somewhat. The EQ belt ultimately undergoes three phases: one where wave activity is dominant and unaffected by the TCs at higher latitudes, one where TCs seem to affect equatorial dynamics, then one where the TC and EQ belts co-exist in equilibrium.

For an objective diagnosis of CCEWs, a wavenumber-frequency power spectrum analysis is developed from the OLR field based on the methodology of Wheeler and Kiladis (1999). The symmetric spectrum shows Kelvin wave modes of wavenumber 2-5 as the dominant wave type (Figure 6d). In addition, a westward-propagating equatorial Rossby wave signal is apparent with equivalent depths between 10-100 m. The asymmetric spectrum features weaker, but widespread high-frequency variability with a westward low-frequency signal that is comparable to the equatorial Rossby waves (not shown). The time-varying wave structure is then analyzed using wavelet decomposition (Torrence and Compo 1998) with a Morlet mother wavelet chosen for the 7.5°S-7.5°N OLR field. Consistent with Figure 6a-d, Figure 6e shows that wave modes with a period between 2-10 days emerge quickly, and are prominent throughout the simulation. However, wave power appears to be somewhat reduced from day 30-40. Indeed, this feature exists across all simulations, marked by a relative minimum in total wave power in the intermediate stages (Figure 6f), which coincides with the strengthening easterly wind shown in Figure 6b. Notably, Figure 6f shows that the time scales of wave development and suppression are dependent on β, as the maxima and minima of wave power are lagged in HALF15 relative to ENHD15.

The vertical structure of the EQ belt in FULL00 is shown in the left panels of Figure 7 in x-z space. Temperature anomaly, zonal wind, and cloud condensate are averaged from 7.5°S-7.5°N.

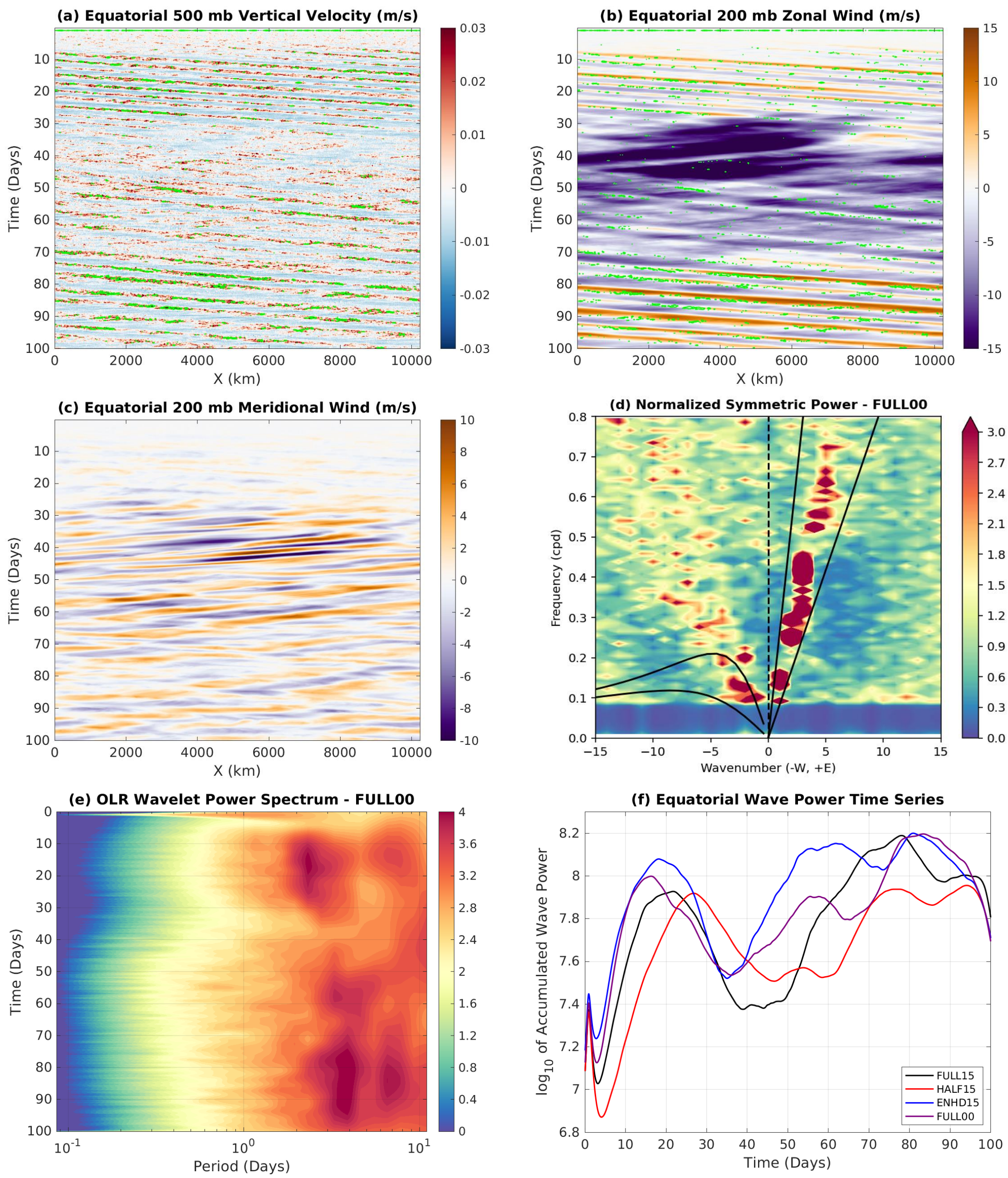

FIG. 6. (a-c) Hovmöller diagrams of 500 hPa vertical velocity, 200 hPa zonal wind, and 200 hPa meridional wind respectively, averaged latitudinally from 7.5°S-7.5°N in FULL00. The 20 mm day^{-1} precipitation rate contour is overlaid on (a-b) in green. (d) Symmetric wavenumber-frequency power spectra of OLR in FULL00, where dispersion curves are plotted at 10 m and 100 m equivalent depth. (e) Time-varying wave power in FULL00, developed from a wavelet analysis of OLR. (f) Accumulated equatorial wave power from the wavelet technique used in (e) for all simulations except FULL45.

At day 20 (Figure 7a), alternating areas of zonal wind convergence and divergence slope westward with height. Low-level convergence and upper-level divergence are in phase with deep, thick clouds. The zonal wind pattern reverses above 12 km, instead sloping eastward with height. This strongly resembles the classic Kelvin wave structure even though no filtering has been applied, again suggesting that Kelvin waves are the dominant mode of self-aggregated convection equatorward of 10°. The convectively active phase is led by anomalous mid-level warmth (Figure 7a) to the east, with relatively cool, moist air trailing to the west in the mid-levels due to rain evaporation (not shown). A long belt of shallow clouds leads the active phase, emerging due to large-scale subsidence in the suppressed phase. This is analogous to the subsiding branch of the overturning circulation associated with SA in non-rotating and weakly rotating f-plane simulations (Muller and Held 2012; Carstens and Wing 2022).

At day 50, easterly winds are dominant throughout the troposphere (Figure 7c), and the distribution of convection is less coherent. Recall from Section 4 that TCs spun up and reached maturity throughout the high-latitude belt of the domain after day 20. During this intermediate time, TCs influence the EQ belt through equatorward transport of easterly momentum from their outflow, visualized as a meridional flux of zonal momentum (Figure 7b). This feature is most pronounced aloft, with convergent upper-tropospheric meridional flow near the equator and mean divergence near the surface, the opposite of a traditional Hadley circulation. This corresponds to greater mean subsidence and less precipitation observed in the EQ belt from days 30-50 (Figure 6a). Shi and Bretherton (2014) note a weak eddy-driven Hadley-type circulation in their GCM configuration, with similar amplification of easterly flow and momentum flux in the first 30 days. As TC activity retreats poleward after day 50 here, the equatorward flux of easterly momentum relaxes (Figure 7d), equatorial waves take control once again, and the structure of the EQ belt again resembles Figure 7a (Figure 7e). It is unclear why lower-latitude TCs become less common in later stages, though it may be related to the stronger background flow relative to the first 30 days. Like other analyses, there is little difference between simulations with differing β, other than the precise timing.

In Figure 7d, the zonal OLR and precipitation structure of the Kelvin wave environment is composited each hour from day 10-30. This composite is centered on the convectively active wave phases, defined as the zonal grid point with the maximum 500 mb vertical velocity averaged from 7.5°S-7.5°N in each third of the domain (assuming a wavenumber-3 structure, which is

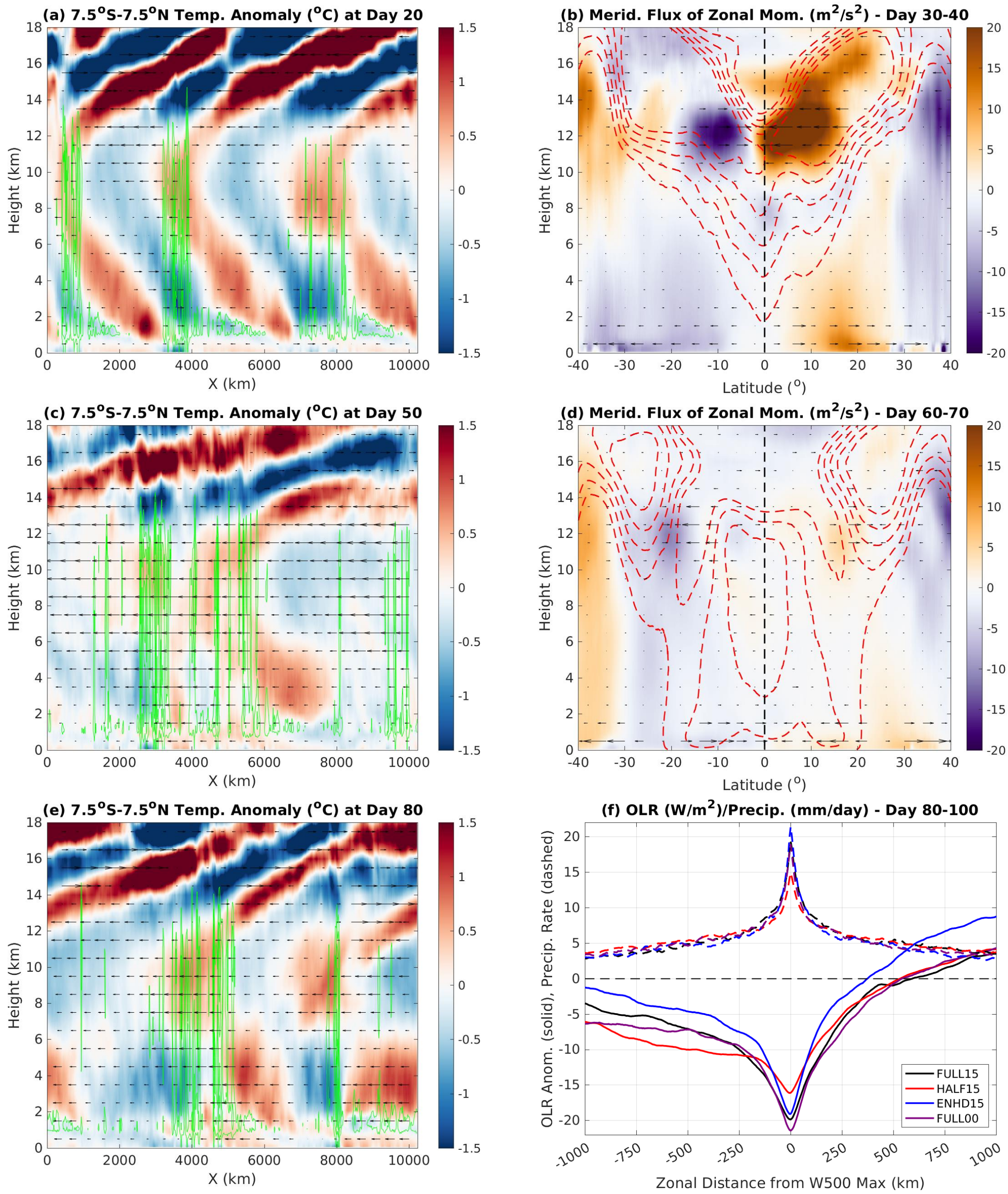

FIG. 7. Left: Cross sections in x-z space of the equatorial belt in FULL00 at (a) day 20, (c) day 50, and (e) day 80, averaged from 7.5°S-7.5°N. Temperature anomaly is shaded, with zonal wind vectors and the 0.04 g kg^{-1} cloud condensate contour overlaid in green. (b) and (d) show the latitudinal and vertical profile of the zonally-averaged meridional flux of zonal momentum in FULL00, time-averaged from day 30-40 and day 60-70, respectively. There, vectors represent the average meridional wind during those times, while red contours represent easterly zonal wind in 2 m s^{-1} increments. (f) shows a zonal cross section of OLR anomaly and precipitation rate through the center of the convectively active wave phase.

most common). The zonal cross section extends 1000 km to the west and east of this point to capture characteristics of the larger-scale environment. The OLR field exhibits zonal asymmetry, with a positive anomaly beyond 300-500 km to the east, despite zonal symmetry in the vertical motion and precipitation fields (Figure 7d). The low clouds leading the convectively active phase enhance radiative cooling while upper-level convergence suppresses deep convection (Figure 7a). The relative symmetry of the precipitation suggests that differences in OLR are driven by shallow, rather than deep convection. Reduced OLR west of the wave maximum is caused by the residual moisture left behind after its passage, and therefore increased absorptivity relative to the east side. Similar meridional profiles reveal that both lower-level and upper-level winds tend to be stronger at the outermost radii (not shown), suggesting that the transition from the EQ to TC regimes is marked by stronger mean flow throughout the troposphere.

6. Discussion

These β-plane simulations were initially motivated by the regime change in convective self-aggregation as a function of f in the f-plane simulations of CW20 and CW22. Essentially, as f increased, the advective feedback in the FMSE variance budget (Equation 2) became more negative, reflecting stronger lateral export of moist static energy from moist convective patches. Beyond a threshold value of f (analogous to about 6° effective latitude in that setting), convection failed to fully consolidate into one coherent cluster. As f continued to increase to a sufficient value, tropical cyclogenesis occurred and served as a driver of further aggregation in the model domain, owing to the TC's strong surface flux and radiative feedbacks.

We see a similar regime transition of SA in these simulations, regardless of the magnitude of β or the domain's central latitude. This is summarized briefly by Figure 3e. Equatorward of 10°, surface flux and shortwave radiative feedbacks successfully counteract a weakly negative advective feedback, and aggregated convection quickly develops in the form of convectively-coupled Kelvin waves. The resulting mode of aggregated convection differs from the f-plane environment, simply due to the fundamental role of β in driving equatorial wave activity. The rapid spontaneous development of CCKWs suggests a mechanistic link between idealized SA and observed synoptic and planetary-scale equatorial convective modes, particularly the strong role of shortwave radiative feedbacks in the maintenance of CCKWs. From 10-15°, the positive surface flux and shortwave feedbacks reduce while the negative advective feedback strengthens. While Figure 3e is a composite mean of all simulations, and there is variation in the minimum latitude of TC genesis with changes in β, a transition from wave-dominated to cyclone-dominated regimes occurs. At progressively higher latitudes, the increased TC density causes increases to the surface flux and longwave radiative feedbacks, and strengthening of the negative advective feedback.

The separation of SA into distinct latitude-dependent regimes is largely consistent with the 1) equatorial no-TC, 2) equatorial sparse-TC, and 3) high-latitude dense-TC regimes found by Chavas and Reed (2019) in aquaplanet GCM simulations with uniform thermal forcing. A numerical comparison is presented in Table 3. In their model, the size distribution of convective entities in the low-latitudes was set by the equatorial Rhines scale ($L_\beta = \frac{\pi}{2}\sqrt{\frac{U_\beta}{\beta}}$), incorporating β under spherical geometry. The high-latitude regime was set by an inverse-f scaling, the ratio of the theoretical TC potential intensity (Emanuel 1986) to f ($L_f = \frac{U_f}{f}$). Under variations in planetary rotation rate or radius, Chavas and Reed (2019) found that the peak genesis (separating regimes 2 and 3) occurred at a value of f that scales with a critical latitude where the Rhines and inverse-f scales met. Using approximate velocity scales of 10 m s^{-1} at low latitudes (typical flow speed in an equatorial wave or pre-TC disturbance) and 80 m s^{-1} at high latitudes (maximum TC intensity) under constant β, the critical latitudes in our simulations are estimated to be 21° (HALF15), 25° (FULL15, FULL45, FULL00), and 34° (ENHD15). These latitudes are higher than the boundaries we defined between our EQ and TC regimes. However, our EQ-TC transition is more closely related to the transition from regimes 1 to 2 in Chavas and Reed (2019), as the minimum latitude of tropical storm occurrence in our simulations marks the transition to a "sparse-TC" regime. Chavas and Reed (2019) predicted that the minimum TC distance from the equator should decrease as β increases, via the Rhines scale equation above. This holds true in our simulations when considering hurricanes (33 m s^{-1}), as while the minimum latitude of hurricane occurrence increases with β, the corresponding Cartesian distance decreases. A crude metric to identify the transition between sparse-TC and dense-TC regimes is presented in Figure S2 of the Supporting Information, where Figure S2f represents the final column of Table 3. Briefly, the sparse-TC regime emerges as a latitudinal local maximum in zonal-mean surface pressure, separated from the more persistent organized convective modes at lower and higher latitudes. The eventual decrease in surface pressure with further increasing latitude in Figure S2f denotes increasing TC density, and can be considered the starting point of a transition to a dense-TC regime. This metric scales with β in the same direction as the Chavas and Reed (2019) critical latitude.

TABLE 3. Summary of comparison between our β-plane simulations and the GCM aquaplanet simulations of Chavas and Reed (2019, CR19). Simulations are listed in order of β as given by the second column. The third column lists the equatorial Rhines scale calculated from β and a 10 m s^{-1} velocity scale for equatorial waves. The fourth column lists the CR19 theoretical critical latitude separating "sparse-TC" and "dense-TC" regimes derived from the aforementioned Rhines scale, and an inverse-f scale using an 80 m s^{-1} velocity scale for TCs. Then, the minimum latitudes of tropical storm (18 m s^{-1} wind) and hurricane (33 m s^{-1}) occurrence are listed. Finally, these are followed by an approximate latitude denoting the transition to a TC-dense regime, based on latitudinal variability in zonal-mean equilibrium surface pressure and shown in Figure S2.

Simulation	β	Rhines Scale	CR19 Critical Latitude	Minimum TS Lat.	Minimum Hurricane Lat.	$dp/d\phi < 0$
HALF15	1.05×10^{-11}	1533 km	21°	9.00°	11.66°	15°
FULL15	1.43×10^{-11}	1314 km	25°	13.99°	20.07°	19°
FULL45	1.43×10^{-11}	1314 km	25°	17.46°	21.87°	24°
FULL00	1.43×10^{-11}	1314 km	25°	17.09°	19.66°	21°
ENHD15	2.55×10^{-11}	984 km	34°	12.60°	24.63°	29°

The equilibrium genesis and track distributions in Figure 4 are useful to compare with aquaplanet and climate model simulations. When normalized to mimic realistic surface area variation with latitude, a preference for genesis in the subtropics appears. Genesis rates are generally smaller than the coarser simulations of Merlis et al. (2016) and Chavas and Reed (2019), though we only consider a 40-day sample in each simulation and use a different genesis definition. While we remove genesis cases within 5° of the meridional boundaries, it is possible that some high-latitude genesis events still stem from pre-existing vorticity maxima which transiently weakened below the 18 m s^{-1} threshold, either through vortex binary interaction or strong vertical wind shear along the boundaries. In this case, purely spontaneous genesis events would have a more robust peak frequency in the subtropics as seen in the prior GCM aquaplanet studies. Nonetheless, TC tracks behave consistently, following a β drift-induced path toward the meridional boundaries (Shi and Bretherton 2014), with number density consistently increasing as a function of latitude. The fraction of seed disturbances that develop into TCs is 40-50% regardless of β. This is similar to the development fraction found by Hsieh et al. (2020) in a GCM with realistic boundary conditions, who suggest that TC behavior follows seed behavior. They find a slightly higher seed development rate in experiments where the meridional SST temperature gradient is reduced (more similar to our simulations), attributing this to changes in the ventilation index. This slight offset is likely influenced by our lower vorticity threshold to determine a disturbance (1×10^{-4} s^{-1} here, compared to 4×10^{-4} s^{-1} there). Hsieh et al. (2020) also find an increase in seed generation with increased planetary rotation rate (simultaneous increases to both f and β), while increasing only β by lowering the planetary radius causes reduced low-latitude seed generation. Both of their findings are in agreement with our ENHD15 simulation, which has the lowest rates of TC genesis equatorward of 25°, and the highest beyond 30°. Chavas and Reed (2019) find an increase in genesis rate as the planetary rotation rate increases and the planetary radius decreases. This aligns with our Figure 4c, where the genesis rate is typically lowest in the HALF15 simulation (lowest β) and highest in ENHD15 and FULL45 (highest β and f). Chavas and Reed (2019) find a more robust quasi-linear dependence of genesis rate on f across their suite of simulations compared to ours, increasing up to subtropical latitudes and decreasing farther poleward. We attribute this difference to a combination of more limited sampling, potential genesis events from pre-existing vortices as discussed above, and greater surface area to accommodate high-latitude TCs in Cartesian geometry. With no near-equatorial genesis events in our simulations, the dynamics of genesis resemble the "high-f" pathway described in CW20 and references therein, and genesis is favored in disturbances that are more humid aloft (Hopsch et al. 2010) and feature stronger radiative heating and surface flux effects (Ruppert et al. 2020; Zhang et al. 2021; Wing 2022).

We simulate higher TC intensities than idealized GCM simulations, which is expected given the much finer resolution. While the bimodal distribution in the lifetime maximum intensity (Figure 4g) is skewed more heavily toward high intensities than in observations (Lee et al. 2016), owing to the idealized environment with no imposed vertical wind shear, a bimodal distribution is captured with peaks at both hurricane and minimal tropical storm intensities. The overall peak TC intensities in the 70-75 m s^{-1} range are comparable with the strongest TCs captured by Fedorov et al. (2018), who demonstrate the potential for downscaling a high-resolution GCM to scales more readily able to resolve eyewall processes. Notably, Fedorov et al. (2018) also find an increasing focus for genesis events in the subtropics and mid-latitudes when their equator-to-pole SST gradient is reduced. A dependence of TC peak intensity on latitude emerges in our simulations, where the most intense TCs at a given latitude are generally weaker as f increases. While many of our

TCs are limited by multi-vortex interactions, Stansfield and Reed (2021) find a thermodynamic basis for such a decrease in their aquaplanet simulations with uniform thermal forcing. There, the potential intensity steadily decreases from 20-50° latitude, in large part due to increases in static stability and ventilation index with latitude. Broadly, our findings reflect favorably on the ability of both parameterized and downscaled GCMs to capture the fundamental dynamics governing large-scale TC behavior. Moving forward, the improved ability for our simulations to resolve strong inner-core winds and heating yields more realistic insight into mesoscale processes in individual TCs compared to GCMs, including radiative and surface flux feedbacks. While we have primarily focused on TC statistics in this study, our simulations cumulatively provide over 150 distinct hurricane tracks, from which an extensive process-oriented analysis of individual genesis and intensity change events can be performed in future work.

7. Conclusions

β-plane simulations were developed to add a layer of complexity to the f-plane environment studied by CW22, permitting the unified study of convective self-aggregation under both weak and strong rotation. This model configuration can be viewed as a computationally expensive but more realistic alternative to "TC World" (Khairoutdinov and Emanuel 2013) due to the inclusion of β and the realistic range of Coriolis parameters. It is also a convection-permitting counterpart to aquaplanet GCM simulations with uniform thermal forcing (Shi and Bretherton 2014; Merlis et al. 2016; Chavas and Reed 2019), though our Cartesian geometry means that all latitudes have an identical surface area, influencing TC statistics. This manuscript focused on three key questions: how do the mechanisms contributing to SA onset and maintenance change as a function of f, how does equilibrium TC behavior vary with f and β, and what are the dominant modes of SA at low latitudes when β is introduced?

Similar to the f-plane simulations studied by CW22, there are two distinct regimes of convective organization here - an equatorial mode dominated by convectively coupled Kelvin waves, transitioning around 10-15° to a high-latitude belt dominated by TCs. A minor difference from the f-plane is the lack of TCs equatorward of 9°, though the TCs at higher effective latitudes on the β-plane generally follow a top-down vortex development similar to the "high-f" genesis regime in CW20. As the magnitude of β changes between these simulations, the Coriolis parameter separating the two regimes, along with the time scales of TC and wave development, vary somewhat. Otherwise, there is notable and somewhat surprising consistency between the various β-plane simulations. SA in the equatorial regime (waves) is largely maintained by shortwave radiative feedbacks, while strong surface flux feedbacks primarily drive organization at high latitudes, particularly once TCs develop. Drying takes place more quickly at low latitudes initially, then after a period of TC spinup between days 10-20, substantial drying ensues between individual TCs due to longwave radiative and surface flux feedbacks. The latitudes of the meridional boundaries have the heaviest influence on the number and distribution of TCs.

The most fundamental difference between non-rotating and "low-f" f-planes with our equatorial belt is that waves are the primary mode of organized convection, rather than circular clusters or non-rotating bands. This is a direct consequence of introducing β, but the same mechanisms driving low-f SA are also relevant processes affecting the moisture variability in the equatorial waves on the β-plane. In this way, radiative and surface flux feedbacks can be considered thermodynamic mechanisms for CCEW maintenance and amplification. The simulations also yield important tropical-extratropical interactions and features of large-scale circulation, despite uniform thermal forcing. A relationship emerges between TC activity and deep-layer equatorial flow. These features, along with our findings on the distribution of TCs and the transition between regimes of organized convection, show noteworthy consistency with similarly-configured GCMs. The finer resolution employed here permits a more detailed study of TCs and advective processes, which are in line with findings on the smaller f-plane. This consistency across model frameworks provides an encouraging outlook for the utility of rotating RCE.

Future work may use this framework to examine the role of the FMSE variance budget feedbacks on wave development, amplification, and propagation through mechanism denial experiments and changes to the thermal forcing. In addition, thorough assessments of TC size, separation distance, intensification, and motion can be developed from the current simulation set. Rapid intensification is an area of particular interest, given the challenges it presents for forecasting and communication. Given the abundance of both CCEWs and TCs, their interactions may also be studied in detail, as Kelvin waves are widely thought to modulate TC activity. Mechanism denial experiments may reveal the importance of surface flux and radiative feedbacks in constraining TC frequency in a controlled setting, an area of ongoing debate in tropical climate change. Performing these simulations using different values of SST can provide a rotating analog to RCEMIP (Wing et al. 2018, 2020). Finally, while the regimes and dominant mechanisms of SA remained consistent from constant to varying f, additional layers of complexity are appropriate to consider, such as SST gradients or diurnally-varying radiation. Such experiments may also employ more complex microphysics than the single-moment package used here, to test how radiative processes may be affected by the choice of scheme. Ultimately, these simulations offer an exciting setting to study numerous convective modes and their multiscale interactions, revealing fundamental processes governing tropical weather and climate in a controlled setting.

Acknowledgments. We acknowledge computing support from Cheyenne (doi: 10.5065/D6RX99HX), provided by NCAR's Computational and Information Systems Laboratory, sponsored by the National Science Foundation. We also acknowledge Marat Khairoutdinov for providing and maintaining the System for Atmospheric Modeling (SAM). JDC thanks Robert Hart, Jeffrey Chagnon, Mark Bourassa, and James Elsner for their support while serving on his doctoral committee, and Allison Brannan for her assistance in performing the wavelet analysis. Wavelet software was provided by C. Torrence and G. Compo, and is available at http://atoc.colorado.edu/research/wavelets. AAW acknowledges funding support from NSF grant 1830724. Finally, we thank Dan Chavas and two anonymous reviewers for their insightful, constructive feedback and additional resources, which greatly improved the manuscript.

Data availability statement. Model input files used to run the simulations, along with post-processed model output data and MATLAB code used to generate figures, are available publicly at https://github.com/jdcarstens17/BetaPlaneRCE

References

Baranowski, D. B., M. K. Flatau, P. J. Flatau, and A. J. Matthews, 2016: Impact of atmospheric convectively coupled equatorial Kelvin waves on upper ocean variability. *J. Geophys. Res. Atmos.*, **121**, 2045–2059, https://doi.org/10.1002/2015jd024150.

Bercos-Hickey, E., and C. M. Patricola, 2021: Anthropogenic influences on the African easterly jet-African easterly wave system. *Clim. Dyn.*, **57**, 2779–2792, https://doi.org/10.1007/s00382-021-05838-1.

Boos, W. R., A. V. Fedorov, and L. Muir, 2016: Convective self-aggregation and tropical cyclogenesis under the hypohydrostatic rescaling. *J. Atmos. Sci.*, **73**, 525–544, https://doi.org/10.1175/jas-d-15-0049.1.

Bretherton, C. S., P. N. Blossey, and M. Khairoutdinov, 2005: An energy-balance analysis of deep convective self-aggregation above uniform SST. *J. Atmos. Sci.*, **62**, 4237–4292, https://doi.org/10.1175/JAS3614.1.

Carstens, J. D., and A. A. Wing, 2020: Tropical cyclogenesis from self-aggregated convection in numerical simulations of rotating radiative-convective equilibrium. *J. Adv. Model. Earth Syst.*, **12**, https://doi.org/10.1029/2019ms002020.

Carstens, J. D., and A. A. Wing, 2022: A spectrum of convective self-aggregation based on background rotation. *J. Adv. Model. Earth Syst.*, **14**, https://doi.org/10.1029/2021ms002860.

Chavas, D. R., and K. A. Reed, 2019: Dynamical aquaplanet experiments with uniform thermal forcing: System dynamics and implications for tropical cyclone genesis and size. *J. Atmos. Sci.*, **76**, 2257–2274, https://doi.org/10.1175/jas-d-19-0001.1.

Clough, S., M. Shephard, E. Mlawer, J. Delamere, M. Iacono, K. Cady-Pereira, S. Boukabara, and P. Brown, 2005: Atmospheric radiative transfer modeling: A summary of the AER codes. *J. Quant. Spectrosc. Radiat. Transfer*, **91**, 233–244, https://doi.org/10.1016/j.jqsrt.2004.05.058.

Coppin, D., and S. Bony, 2015: Physical mechanisms controlling the initiation of convective self-aggregation in a general circulation model. *J. Adv. Model. Earth Syst.*, **7**, 2060–2078, https://doi.org/10.1002/2015ms000571.

Craig, G. C., and J. M. Mack, 2013: A coarsening model for self-organization of tropical convection. *J. Geophys. Res.*, **118**, 8761–8769, https://doi.org/10.1002/jgrd.50674.

Cronin, T. W., and D. R. Chavas, 2019: Dry and semidry tropical cyclones. *J. Atmos. Sci.*, **76**, 2193–2212, https://doi.org/10.1175/jas-d-18-0357.1.

Davis, C. A., 2015: The formation of moist vortices and tropical cyclones in idealized simulations. *J. Atmos. Sci.*, **72**, 3499–3516, https://doi.org/10.1175/jas-d-15-0027.1.

Emanuel, K. A., 1986: An air-sea interaction theory for tropical cyclones. Part 1: Steady state maintenance. *J. Atmos. Sci.*, **43**, 585–604, https://doi.org/10.1175/1520-0469(1986)043⟨0585:aasitf⟩2.0.co;2.

Emanuel, K. A., 2003: Tropical cyclones. *Ann. Rev. Earth Planet. Sci.*, **31**, 75–104.

Emanuel, K. A., and D. S. Nolan, 2004: Tropical cyclone activity and the global climate system. *26th Conference on Hurricanes and Tropical Meteorology*, 240–241.

Fang, J., and F. Zhang, 2012: Effect of beta shear on simulated tropical cyclones. *Mon. Wea. Rev.*, **140**, 3327–3346, https://doi.org/10.1175/mwr-d-10-05021.1.

Fedorov, A. V., L. Muir, W. R. Boos, and J. Studholme, 2018: Tropical cyclogenesis in warm climates simulated by a cloud system resolving model. *Clim. Dyn.*, **52**, 107–127, https://doi.org/10.1007/s00382-018-4134-2.

Fu, D., P. Chang, C. M. Patricola, and R. Saravanan, 2019: High-resolution tropical channel model simulations of tropical cyclone climatology and intraseasonal-to-interannual variability. *J. Climate*, **32**, 7871–7895, https://doi.org/10.1175/jcli-d-19-0130.1.

Fu, D., P. Chang, C. M. Patricola, R. Saravanan, X. Liu, and H. E. Beck, 2021: Central American mountains inhibit eastern North Pacific seasonal tropical cyclone activity. *Nature Comm.*, **12**, 1–11, https://doi.org/10.1038/s41467-021-24657-w.

Gill, A., 1982: *Atmosphere-ocean dynamics*. International Geophysics Series, Academic Press.

Held, I. M., R. S. Hemler, and V. Ramaswamy, 1993: Radiative-convective equilibrium with explicit two-dimensional moist convection. *J. Atmos. Sci.*, **50**, 3909–3927, https://doi.org/10.1175/1520-0469(1993)050⟨3909:rcewet⟩2.0.co;2.

Held, I. M., and M. Zhao, 2008: Horizontally homogeneous rotating radiative-convective equilibrium at GCM resolution. *J. Atmos. Sci.*, **65**, 2003–2013, https://doi.org/10.1175/2007jas2604.1.

Hohenegger, C., and B. Stevens, 2016: Coupled radiative-convective equilibrium simulations with explicit and parameterized convection. *J. Adv. Model. Earth Syst.*, **8**, 1468–1482, https://doi.org/10.1002/2016ms000666.

Holland, G. J., 1983: Tropical cyclone motion: Environmental motion plus a beta effect. *J. Atmos. Sci.*, **40**, 328–342, https://doi.org/10.1175/1520-0469(1983)040⟨0328:TCMEIP⟩2.0.CO;2.

Holloway, C. E., and S. J. Woolnough, 2016: The sensitivity of convective aggregation to diabatic processes in idealized radiative-convective equilbrium simulations. *J. Adv. Model. Earth Syst.*, **8**, 166–195, https://doi.org/10.1002/2015ms000511.

Hopsch, S. B., C. D. Thorncroft, and K. R. Tyle, 2010: Analysis of African easterly wave structures and their role in influencing tropical cyclogenesis. *Mon. Wea. Rev.*, **138**, 1399–1419, https://doi.org/10.1175/2009mwr2760.1.

Houze, R. A., 2004: Mesoscale convective systems. *Rev. Geophys.*, **42**, RG4003, https://doi.org/10.1029/2004rg000150.

Hsieh, T. L., G. A. Vecchi, W. Yang, I. M. Held, and S. T. Garner, 2020: Large-scale control on the frequency of tropical cyclones and seeds: A consistent relationship across a hierarchy of global atmospheric models. *Clim. Dyn.*, **55**, 3177–3196, https://doi.org/10.1007/s00382-020-05446-5.

Iacono, M., J. Delamere, E. Mlawer, M. Shephard, S. Clough, and W. Collins, 2008: Radiative forcing by long-lived greenhouse gases: Calculations with the AER radiative transfer models. *J. Geophys. Res.*, **113**, D13 103, https://doi.org/10.1029/2008jd009944.

Khairoutdinov, M. F., and K. A. Emanuel, 2010: Aggregation of convection and the regulation of tropical climate. *29th Conference on Hurricanes and Tropical Meteorology*.

Khairoutdinov, M. F., and K. A. Emanuel, 2013: Rotating radiative-convective equilibrium simulated by a cloud-resolving model. *J. Adv. Model. Earth Sys.*, **5**, 816–825, https://doi.org/10.1002/2013MS000253.

Khairoutdinov, M. F., and D. A. Randall, 2003: Cloud resolving modeling of the ARM summer 1997 IOP: Model formulation, results, uncertainties, and sensitivities. *J. Atmos. Sci.*, **60**, 607–625, https://doi.org/10.1175/1520-0469(2003)060⟨0607:crmota⟩2.0.co;2.

Kiladis, G. N., M. C. Wheeler, P. T. Haertel, K. H. Straub, and P. E. Roundy, 2009: Convectively coupled equatorial waves. *Rev. Geophys.*, **47**, https://doi.org/10.1029/2008rg000266.

Lee, C.-Y., M. K. Tippett, A. H. Sobel, and S. J. Camargo, 2016: Rapid intensification and the bimodal distribution of tropical cyclone intensity. *Nature Comm.*, **7**, 10 625, https://doi.org/10.1038/ncomms10625.

Lu, K. Y., and D. R. Chavas, 2022: Tropical cyclone size is strongly limited by the Rhines scale: Experiments with a barotropic model. *J. Atmos. Sci.*, **79**, 2109–2124, https://doi.org/10.1175/jas-d-21-0224.1.

Madden, R. A., and P. R. Julian, 1971: Detection of a 40–50 day oscillation in the zonal wind in the tropical Pacific. *J. Atmos. Sci.*, **28**, 702–708, https://doi.org/10.1175/1520-0469(1971)028⟨0702:doadoi⟩2.0.co;2.

Manabe, S., and R. F. Strickler, 1964: Thermal equilibrium of the atmosphere with a convective adjustment. *J. Atmos. Sci.*, **21**, 361–385, https://doi.org/10.1175/1520-0469(1964)021⟨0361:teotaw⟩2.0.co;2.

Matsuno, T., 1966: Quasi-geostrophic motions in the equatorial area. *J. Meteorol. Soc. Japan*, **44**, 25–43, https://doi.org/10.2151/jmsj1965.44.1_25.

Merlis, T. M., W. Zhou, I. M. Held, and M. Zhao, 2016: Surface temperature dependence of tropical cyclone-permitting simulations in a spherical model with uniform thermal forcing. *Geophys. Res. Lett.*, **43**, 2859–2865, https://doi.org/10.1002/2016gl067730.

Mlawer, E., S. Taubman, P. Brown, M. Iacono, and S. Clough, 1997: Radiative transfer for inhomogeneous atmospheres: RRTM, a validated correlated-k model for the longwave. *J. Geophys. Res.*, **102**, 16 663–16 682, https://doi.org/10.1029/97jd00237.

Muller, C. J., and I. M. Held, 2012: Detailed investigation of the self-aggregation of convection in cloud-resolving simulations. *J. Atmos. Sci.*, **69**, 2551–2565, https://doi.org/10.1175/jas-d-11-0257.1.

Muller, C. J., and D. M. Romps, 2018: Acceleration of tropical cyclogenesis by self-aggregation feedbacks. *Proc. Nat. Acad. Sci.*, **115**, 2930–2935, https://doi.org/10.1073/pnas.1719967115.

Nolan, D. S., E. D. Rappin, and K. A. Emanuel, 2007: Tropical cyclogenesis sensitivity to environmental parameters in radiative-convective equilibrium. *Q. J. R. Meteorol. Soc.*, **133**, 2085–2107, https://doi.org/10.1002/qj.170.

Patrizio, C. R., and D. A. Randall, 2019: Sensitivity of convective self-aggregation to domain size. *J. Adv. Model. Earth Syst.*, **11**, 1995–2019, https://doi.org/10.1029/2019ms001672.

Ramirez Reyes, A., and D. Yang, 2021: Spontaneous cyclogenesis without radiative and surface flux feedbacks. *J. Atmos. Sci.*, **78**, 4169–4184, https://doi.org/10.1175/JAS-D-21-0098.1.

Ramsay, H. A., M. S. Singh, and D. R. Chavas, 2020: Response of tropical cyclone formation and intensification rates to climate warming in idealized simulations. *J. Adv. Model. Earth Syst.*, **12**, https://doi.org/10.1029/2020ms002086.

Reed, K. A., and D. R. Chavas, 2015: Uniformly rotating global radiative-convective equilibrium in the Community Atmosphere Model, version 5. *J. Adv. Model. Earth Sys.*, **7**, 1938–1955, https://doi.org/10.1002/2015MS000519.

Ruppert, J. H., A. A. Wing, X. Tang, and E. L. Duran, 2020: The critical role of cloud-infrared radiation feedback in tropical cyclone development. *Proc. Nat. Acad. Sci.*, **117**, 27 884–27 892, https://doi.org/10.1073/pnas.2013584117.

Satoh, M., B. Stevens, F. Judt, M. Khairoutdinov, S.-J. Lin, W. M. Putman, and P. Duben, 2019: Global cloud-resolving models. *Curr. Clim. Change Rep.*, **5**, 172–184, https://doi.org/10.1007/s40641-019-00131-0.

Shi, X., and C. S. Bretherton, 2014: Large-scale character of an atmosphere in rotating radiative-convective equilibrium. *J. Adv. Model. Earth Syst.*, **6**, 616–629, https://doi.org/10.1002/2014ms000342.

Stansfield, A. M., and K. A. Reed, 2021: Tropical cyclone precipitation response to surface warming in aquaplanet simulations with uniform thermal forcing. *J. Geophys. Res. Atmos.*, **126**, https://doi.org/10.1029/2021jd035197.

Tang, B. H., and K. A. Emanuel, 2012: Sensitivity of tropical cyclone intensity to ventilation in an axisymmetric model. *J. Atmos. Sci.*, **69**, 2394–2413, https://doi.org/10.1175/jas-d-11-0232.1.

Tompkins, A., and G. Craig, 1998: Radiative-convective equilibrium in a three-dimensional cloud-ensemble model. *Q. J. R. Meteorol. Soc.*, **124**, 2073–2097, https://doi.org/10.1256/smsqj.55012.

Torrence, C., and G. P. Compo, 1998: A practical guide to wavelet analysis. *Bull. Amer. Met. Soc.*, **79**, 61–78, https://doi.org/10.1175/1520-0477(1998)079⟨0061:apgtwa⟩2.0.co;2.

Vu, T. A., C. Kieu, D. R. Chavas, and Q. Wang, 2021: A numerical study of the global formation of tropical cyclones. *J. Adv. Model. Earth Syst.*, **13**, https://doi.org/10.1029/2020ms002207.

Wang, Y., C. A. Davis, and Y. Huang, 2019: Dynamics of lower-tropospheric vorticity in idealized simulations of tropical cyclone formation. *J. Atmos. Sci.*, **76**, 707–727, https://doi.org/10.1175/jas-d-18-0219.1.

Wheeler, M., and G. N. Kiladis, 1999: Convectively coupled equatorial waves: Analysis of clouds and temperature in the wavenumber-frequency domain. *J. Atmos. Sci.*, **56**, 374–399, https://doi.org/10.1175/1520-0469(1999)056⟨0374:ccewao⟩2.0.co;2.

Windmiller, J. M., and G. C. Craig, 2019: Universality in the spatial evolution of self-aggregation of tropical convection. *J. Atmos. Sci.*, **76**, 1677–1696, https://doi.org/10.1175/jas-d-18-0129.1.

Wing, A. A., 2019: Self-aggregation of deep convection and its implications for climate. *Curr. Clim. Change Rep.*, **5**, 1–11, https://doi.org/10.1007/s40641-019-00120-3.

Wing, A. A., 2022: Acceleration of tropical cyclone development by cloud-radiative feedbacks. *J. Atmos. Sci.*, **79**, 2285–2305, https://doi.org/10.1175/jas-d-21-0227.1.

Wing, A. A., S. J. Camargo, and A. H. Sobel, 2016: Role of radiative-convective feedbacks in spontaneous tropical cyclogenesis in idealized numerical simulations. *J. Atmos. Sci.*, **73**, 2633–2642, https://doi.org/10.1175/JAS-D-15-0380.1.

Wing, A. A., and T. W. Cronin, 2016: Self-aggregation of convection in long channel geometry. *Q. J. R. Meteorol. Soc.*, **142**, 1–15, https://doi.org/10.1002/qj.2628.

Wing, A. A., and K. A. Emanuel, 2014: Physical mechanisms controlling self-aggregation of convection in idealized numerical modeling simulations. *J. Adv. Model. Earth. Syst.*, **6**, 59–74, https://doi.org/10.1002/2013ms000269.

Wing, A. A., K. A. Reed, M. Satoh, B. Stevens, S. Bony, and T. Ohno, 2018: Radiative-Convective Equilibrium Model Intercomparison Project. *Geosci. Model Dev.*, **11**, 793–813, https://doi.org/10.5194/gmd-11-793-2018.

Wing, A. A., C. L. Stauffer, T. Becker, K. A. Reed, M. S. Ahn, and e. a. Arnold, N. P., 2020: Clouds and convective self-aggregation in a multimodel ensemble of radiative-convective equilibrium simulations. *J. Adv. Model. Earth. Syst.*, **12**, https://doi.org/10.1029/2020ms002138.

Yanase, T., S. Nishizawa, H. Miura, T. Takemi, and H. Tomita, 2020: New critical length for the onset of self-aggregation of moist convection. *Geophys. Res. Lett.*, **47**, https://doi.org/10.1029/2020gl088763.

Yang, D., 2018a: Boundary layer diabatic processes, the virtual effect, and convective self-aggregation. *J. Adv. Model. Earth Syst.*, **10**, 2163–2176, https://doi.org/10.1029/2017ms001261.

Yang, D., 2018b: Boundary layer height and buoyancy determine the horizontal scale of convective self-aggregation. *J. Atmos. Sci.*, **75**, 469–478, https://doi.org/10.1175/jas-d-17-0150.1.

Zhang, B., B. J. Soden, G. A. Vecchi, and W. Yang, 2021: The role of radiative interactions in tropical cyclone development under realistic boundary conditions. *J. Climate*, **34**, 2079–2091, https://doi.org/10.1175/jcli-d-20-0574.1.

Zhou, W., I. M. Held, and S. T. Garner, 2014: Parameter study of tropical cyclones in rotating radiative-convective equilibrium with column physics and resolution of a 25 km GCM. *J. Atmos. Sci.*, **71**, 1058–1068, https://doi.org/10.1175/jas-d-13-0190.1.

Zhou, W., I. M. Held, and S. T. Garner, 2017: Tropical cyclones in rotating radiative-convective equilibrium with coupled SST. *J. Atmos. Sci.*, **74**, 879–892, https://doi.org/10.1175/jas-d-16-0195.1.